

This is an Open Access document downloaded from ORCA, Cardiff University's institutional repository:<https://orca.cardiff.ac.uk/id/eprint/108292/>

This is the author's version of a work that was submitted to / accepted for publication.

Citation for final published version:

Yu, Siyu, Yang, Nianjun, Vogel, Michael, Mandal, Soumen , Williams, Oliver A. , Jiang, Siyu, Schönherr, Holger, Yang, Bing and Jiang, Xin 2018. Battery-like supercapacitors from vertically aligned carbon nanofiber coated diamond: design and demonstrator. *Advanced Energy Materials* 8 (12) , 1702947. 10.1002/aenm.201702947

Publishers page: <http://dx.doi.org/10.1002/aenm.201702947>

Please note:

Changes made as a result of publishing processes such as copy-editing, formatting and page numbers may not be reflected in this version. For the definitive version of this publication, please refer to the published source. You are advised to consult the publisher's version if you wish to cite this paper.

This version is being made available in accordance with publisher policies. See <http://orca.cf.ac.uk/policies.html> for usage policies. Copyright and moral rights for publications made available in ORCA are retained by the copyright holders.



1 DOI: 10.1002/ ((please add manuscript number))

2 **Article type: Full Paper**

3

4

5 **Battery-like Supercapacitors from Vertically Aligned Carbon Nanofibers Coated**
6 **Diamond: Design and Demonstrator**

7

8 *Siyu Yu, Nianjun Yang,* Michael Vogel, Soumen Mandal, Oliver A. Williams, Siyu Jiang,*
9 *Holger Schönherr, Bing Yang, and Xin Jiang**

10

11 S. Yu, Dr. N. Yang, Dr. M. Vogel, Prof. X. Jiang

12 Institute of Materials Engineering, University of Siegen, 57076 Siegen, Germany

13 E-mail: nianjun.yang@uni-siegen.de, xin.jiang@uni-siegen.de

14 Dr. S. Mandal, Prof. O. A. Williams

15 School of Physics and Astronomy, Cardiff University, Cardiff CF24 3AA, UK

16 S. Jiang, Prof. H. Schönherr

17 Physical Chemistry I, Department of Chemistry and Biology & Research Center of Micro and
18 Nanochemistry and Engineering (Cμ), University of Siegen, 57076 Siegen, Germany

19 Dr. B. Yang

20 Shenyang National Laboratory for Materials Science, Institute of Metal Research (IMR),
21 Chinese Academy of Sciences (CAS), No.72 Wenhua Road, Shenyang 110016 China

22

23 **Keywords:** battery-like supercapacitor, vertically aligned carbon nanofibers, diamond,
24 supercapacitors performance, demonstrator

25

26 To fabricate battery-like supercapacitors with high power and energy densities, big

27 capacitances as well as long-term capacitance retention, vertically aligned carbon nanofibers

28 (CNFs) grown on boron doped diamond (BDD) films are employed as the capacitor

29 electrodes. They possess large surface areas, high conductivity, high stability, and importantly

30 are free of binder. The large surface areas result from their porous structures. The containment

31 of graphene layers and copper metal catalysts inside CNFs leads to their high conductivity.

32 Both electrical double layer capacitors (EDLCs) in inert solution and pseudocapacitors (PCs)

33 using $\text{Fe}(\text{CN})_6^{3-/4-}$ redox-active electrolytes are constructed with three- and two-electrode

34 systems. The assembled two-electrode symmetrical supercapacitor devices exhibit

35 capacitances of 30 and 48 mF cm^{-2} at 10 mV s^{-1} for EDLC and PC devices, respectively. They

36 remain constant even after 10 000 charging/discharging cycles. The power densities are 27.3

37 kW kg^{-1} and 25.3 kW kg^{-1} for EDLC and PC devices, together with their energy densities of

38 22.9 Wh kg^{-1} and 44.1 Wh kg^{-1} , respectively. The performance of these devices is superior to

39 most of reported supercapacitors and batteries. Vertically aligned CNFs/BDD hybrid films are
40 thus useful to construct high-performance battery-like and industry-orientated supercapacitors
41 for future power devices.

42

43 **1. Introduction**

44 Battery-like supercapacitors refer to these electrochemical capacitors (ECs) that possess the
45 features of both ECs (e.g., high power density, P) and batteries (e.g., high energy density, E),
46 as well as big capacitances (C) and long capacitance retention. These ECs meet the demands
47 for powering future multifunctional electronics, hybrid electric vehicles, and industrial
48 equipment.^[1] The construction of such battery-like supercapacitors is thus becoming the core
49 activity of EC researches in recent years.

50 To fabricate battery-like supercapacitors, the first issue to be considered is the choice of
51 suitable capacitor electrodes. Besides large surface areas, it is essential for them to facilitate
52 high electron and ion mobilities. To produce capacitor electrodes with such properties, several
53 strategies have been proposed^[2] by means of 1) improving the conductivity of the electrodes;
54 2) employing nano-sized electrode materials to reduce the diffusion length and meanwhile to
55 enhance the surface areas; 3) utilizing three-dimensional (3D) materials to realize ion
56 diffusion in multiple directions (e.g., porous materials); and 4) reducing the diffusion
57 activation energy of the ions. In these studies, various carbon materials with different
58 hybridization of atomic orbitals (sp^2 and sp^3), different allotropes of carbon (e.g. fullerenes,
59 nanotubes, graphene and diamond etc.), and various dimensionalities (e.g., 0 to 3D) have been
60 intensively investigated.^[3] For most ECs in these approaches, carbon materials have to be
61 mixed with organic binders (e.g., polytetrafluoroethylene^[4]) and further pressed or coated on
62 an electrode supporter (a current collector). Due to the low conductivity and relatively poor
63 stability of these organic binders, both electron mobility inside the formed capacitor
64 electrodes and ion diffusion on the surface of these capacitor electrodes are partially hindered.

65 In most cases, the theoretically expected performance of the fabricated ECs has not been
66 observed. Therefore, novel capacitor electrodes, namely binder-free carbon capacitor
67 electrodes, are highly needed for the construction of battery-like supercapacitors.

68 The second crucial issue for the construction of battery-like supercapacitors is the
69 selection of the electrolytes. For example, inert electrolytes are widely employed for the
70 formation of electrical double layer capacitors (EDLCs). In these solutions, redox species
71 coated conductive substrates with polymer and metal oxides are also employed as the
72 capacitor electrodes to produce pseudocapacitors (PCs).^[5] An alternative, but more efficient
73 approach to construct PCs is to introduce soluble redox species into the electrolyte.^[6] One of
74 the main advantages of this novel approach is that the amount of redox species, which
75 determines the charge storage capacity, is easy to be controlled. However, the contribution of
76 soluble redox electrolytes to the performance of ECs has not been clearly clarified.^[7]
77 Therefore, the development of battery-like supercapacitors in both inert and redox electrolytes
78 should be conducted.

79 We are thus interested in the growth of a novel binder-free carbon capacitor electrode as
80 well as its employment for the construction of battery-like supercapacitors, including EDLCs
81 in inert electrolytes and PCs in redox electrolytes. The binder-free carbon capacitor electrode
82 is constructed using boron doped diamond (BDD) as the electrode supporter and vertically
83 aligned carbon nanofibers (CNFs) as the active electrode materials. The CNFs are directly
84 grown on BDD with a thermal chemical vapor deposition (TCVD) process (**Figure S1**).
85 Namely, such a TCVD process eliminates the need to use low conductive organic binders. For
86 such growth, C_2H_2 is employed as the reaction gas. The copper (Cu) thin film sputtered with a
87 physical vapor deposition (PVD) device acts as the catalyst. Moreover, in this way the CNFs
88 are covalently bonded to BDD via stable C-C bonds, i.e. the CNFs on diamond exhibit good
89 adhesion, increased conductivity, and long-term stability. Furthermore, the CNFs feature high
90 electrical conductivity, large specific surface area, good chemical stability, and 3D porous

91 structures.^[8] Abundant diffusion channels and plenty of active sites are thus expected to be
92 available for our capacitor electrode. Therefore, the hybrid structure of CNFs/BDD films will
93 offer integrated properties of both carbon materials used and resolve the key bottlenecks for
94 the construction of battery-like supercapacitors mentioned above.

95 In this contribution, we first present the details about the growth of vertically aligned
96 CNFs on BDD, followed by the characterization of their morphology, chemical structure and
97 wettability using SEM, TEM, XPS, Raman, and water contact angle measurements. The
98 construction of ECs with CNFs/BDD hybrid films as the capacitor electrodes is then shown.
99 Using both three- and two-electrode configurations, their performance is evaluated in the inert
100 solution (1.0 M H₂SO₄) as well as in the redox species contained electrolyte (1.0 M Na₂SO₄ +
101 0.05 M Fe(CN)₆^{3-/4-}). At last, a stand-alone supercapacitor is demonstrated.

102

103 **2. Results and Discussion**

104 **2.1. Design of CNFs/BDD Capacitor Electrodes**

105 A good capacitor electrode features high electrical conductivity, a large specific surface area,
106 good chemical stability, and a 3D porous structure. CNFs grown on BDD are believed to be
107 the potential candidates since it has been shown that in a TCVD technique the growth (e.g.,
108 size, length, density) of CNFs is actually determined by the thickness of a catalyst (in our case,
109 the Cu film).^[9] To fabricate such a capacitor electrode, the growth of CNFs grown on BDD
110 was first optimized. The SEM images of Cu films sputtered on BDD with different sputtering
111 times ($t_{\text{Cu,s}}$) of 15, 30, 60, 90, and 120s were thus recorded. **Figure 1a** shows one typical SEM
112 image of a Cu film with $t_{\text{Cu,s}}$ of 60 s. The SEM images of Cu films with $t_{\text{Cu,s}}$ of 15, 30, 90, and
113 120 s are shown in **Figure S2**. In all these images, BDD films are fully covered with Cu. The
114 thicknesses of Cu films vary from a dozen to tens of nanometers, increasing as a function of
115 $t_{\text{Cu,s}}$. With $t_{\text{Cu,s}}$ from 15 to 90 s, the crystal boundaries of BDD can be clearly observed, but
116 become indistinct once $t_{\text{Cu,s}}$ is up to 120 s. These Cu films were then applied as the catalyst for

117 the growth of CNFs. The surface morphologies of as-grown CNFs/BDD hybrid films were
118 then checked using SEM. As an example, the SEM images in top and side views for $t_{\text{Cu,s}}$ of 60
119 s are shown in **Figure 1b**. Those for $t_{\text{Cu,s}}$ of 15, 30, 90, and 120 s are shown in **Figure S3**. For
120 $t_{\text{Cu,s}}$ of 15 s, the growth of CNFs is random. While CNFs are quasi vertically aligned when
121 $t_{\text{Cu,s}}$ is up to 30 s. When $t_{\text{Cu,s}}$ is longer than 60s, vertically aligned CNFs with much denser
122 arrangement are acquired. The thicknesses of CNFs (insets in SEM images) are measured to
123 be about 2.5, 2.8, 3.6, 4.3, and 5.0 μm for $t_{\text{Cu,s}}$ of 15, 30, 60, 90, and 120 s, respectively.
124 Interestingly, all CNF films exhibit 3D porous properties. Lots of channels or pores exist
125 between CNFs, even for the CNFs with $t_{\text{Cu,s}}$ longer than 60 s. This is partially because the
126 growth direction of CNFs is perpendicular to the substrate. The surface morphology of CNF
127 films is closely dependent on that of the substrate. For instance, the surface characteristic of
128 the CNF film for $t_{\text{Cu,s}}$ of 60 s (**Figure 1b**) shows actually the morphology of BDD surface. At
129 some irregular crystal boundaries of BDD, tilted CNFs are then obtained and pores are
130 generated. Such a statement is further supported by the control experiments using a smooth Si
131 substrate as the supporter for the growth of CNFs. In this case, only a smooth surface of the
132 CNF films was obtained under identified conditions (**Figure S4**).

133 To figure out the effect of the morphology of Cu catalysts on the growth of CNFs on BDD,
134 the growth of CNFs using Cu particles as catalyst was further tested. These Cu particles were
135 generated via annealing the Cu films at 500 °C for 60 min (**Figure S5**). Vertically aligned
136 CNFs are gained with $t_{\text{Cu,s}}$ of 90 and 120 s (**Figure S6**). Interestingly, the thicknesses of CNF
137 films are slightly smaller than those CNFs films obtained without annealing (WOA) of the Cu
138 films. More details can be found in the experimental session of the supporting information.
139 Therefore, the copper films WOA were used throughout our studies.

140

141 **DFG Proposal**

142

143 **Title:** Electrochemical Reduction of CO₂ into C₂ Chemicals Using Hybrid Electrocatalysts
144 of Doped Diamond and Metal-Organic Frameworks

145

146 **Applicant:** Dr. Nianjun Yang, Institute of Materials Engineering, University of Siegen

147

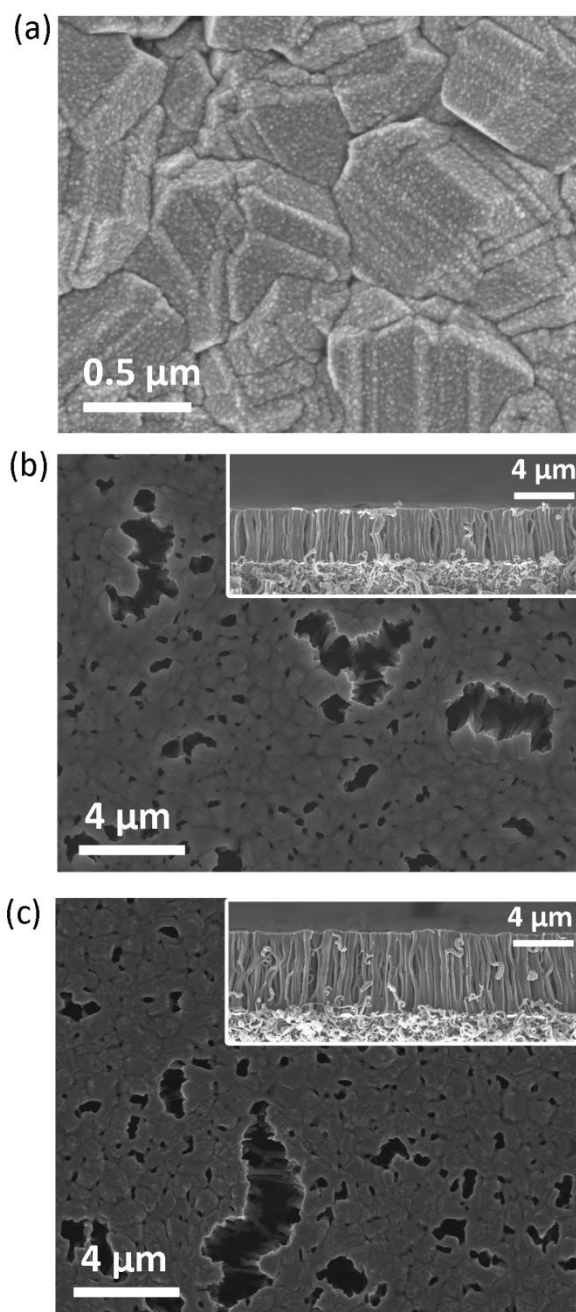
148 **Duration:** 36 months

149

150 **Abstract:** Electrochemical reduction of carbon dioxide (ECCO₂R) into useful chemicals and
151 liquid fuels is of scientific significance and industrial importance. Especially, ECCO₂R into C₂
152 chemicals is highly demanded because industrial synthesis of C₂ chemicals is usually more
153 complicated and energy intensive than that of C₁ ones. However, only C₁ reduction products
154 are obtained on most electrocatalysts. Therefore, we propose in this project the
155 employment of hybrid electrocatalysts for the realization of highly efficient, selective, and
156 stable reduction of CO₂ into C₂ chemicals in aqueous solutions. The hybrid electrocatalysts
157 consist of doped diamond and metal-organic frameworks (MOFs). Doped diamond is chosen
158 in that on this non-metal electrocatalyst ECCO₂R into C₂ chemicals is possible. It also
159 features high stability at negative potentials and minimized degree of hydrogen evolution
160 during ECCO₂R. Selective production of C₂ chemicals during ECCO₂R will be realized through
161 controlling and altering the type and density of catalytic sites, namely nitrogen- and/or
162 boron- doped sp³ carbon atoms. Moreover, three-dimensional (3D) diamond will be
163 fabricated and further coated with porous MOFs. Then the surficial concentration of CO₂ will
164 be enhanced, leading to improved faradic efficiencies for selective ECCO₂R into C₂ chemicals.
165 Furthermore, the synergistic effects of MOFs and 3D-BNDD are expected during the
166 formation of C₂ chemicals (namely C-C bonds) from the intermediates generated on both
167 doped diamond and MOFs. In addition, such a hybrid electrocatalyst will have improved
168 stability, especially MOFs. The 3D boron- and nitrogen- doped diamond (BNDD) will be
169 fabricated through either a top-down etching of a BNDD film with a nickel hard mask or a
170 bottom-up overgrowth of SiO₂ sphere templates with BNDD films. The type and density of
171 boron- and/or nitrogen- doped sp³ carbon atoms will be varied during microwave plasma
172 enhanced chemical vapor deposition processes. MOFs will be electrochemically deposited
173 on 3D diamond by means of a reductive approach. CO₂ surficial concentrations will be
174 calculated using quartz crystal microbalance. Its variation will be realized through changing
175 the morphology and composition of MOFs. Their synthesis is thus conducted with different
176 precursors and at different potentials. The reduction products will be detected using high
177 performance liquid chromatogram, gas chromatogram, and related techniques. Based on
178 the type and amount of monitored reduction products, the faradaic efficiencies and
179 selectivity of ECCO₂R into C₂ chemicals will be evaluated for different hybrid
180 electrocatalysts. Besides the investigation of the stability of hybrid electrocatalysts at
181 different reduction potentials for long electrolysis times, the synergistic effects between

182 MOFs and 3D-BNDD will be cleared. The reduction pathways for efficient and stable ECCO₂R
183 into selective C₂ chemicals will be proposed based on the results by use of in situ
184 spectroelectrochemical techniques, electrochemical methods, and density functional
185 theory simulations.

186



187
188 **Figure 1.** Characterization: SEM images of (a) a Cu film on BDD, (b) a CNF film on BDD
189 with a growth time of 60 min, (c) a CNF film with a growth time of 90 min. The time for Cu
190 sputtering was 60 s. The inset images show the cross sections of as-grown CNFs.

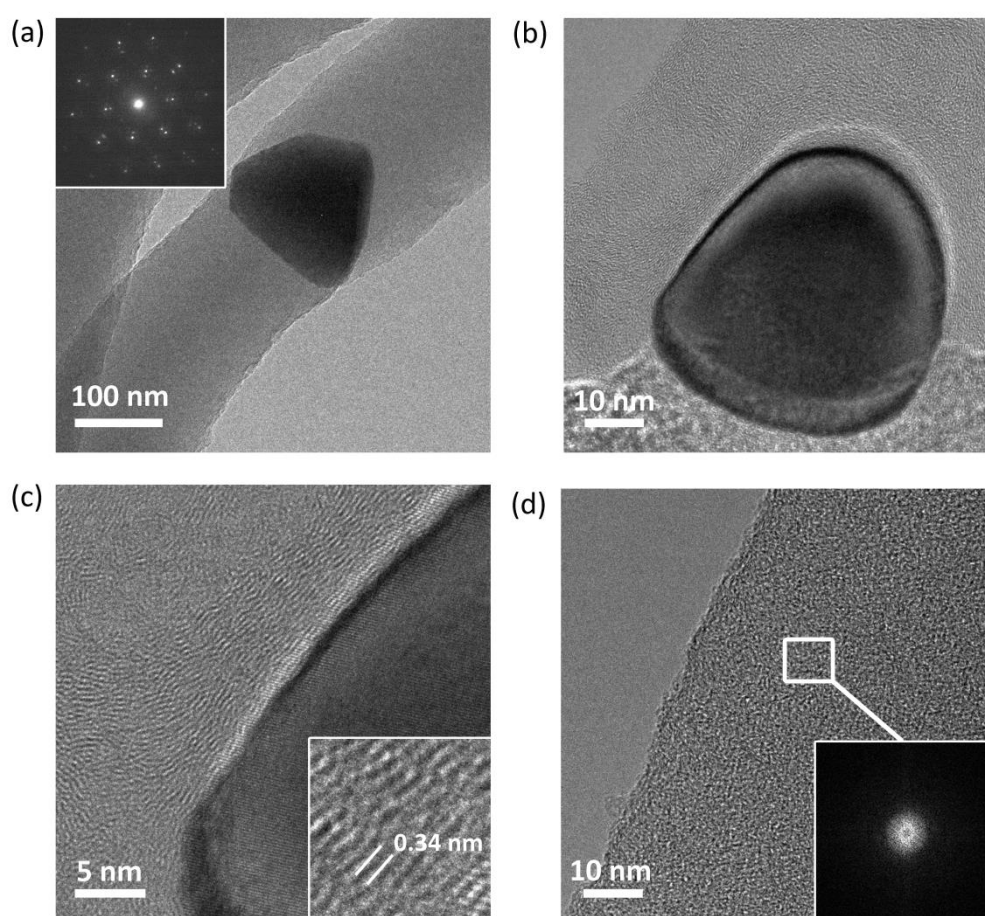
191
192 Obviously, altering the growth time leads to the formation of CNFs with various lengths.
193 In a case study, Cu films sputtered with $t_{\text{Cu,s}}$ of 60 s WOA were applied for the growth of
194 CNFs using different growth times. The SEM images of CNFs grown using a growth time of
195 30, 60, 90, and 120 min are shown in **Figure S7a**, **Figure 1b**, **Figure 1c**, and **Figure S7b**,
196 respectively. As expected, the surface morphologies of these CNFs/BDD hybrid films are
197 almost identical. The lengths of CNFs are about 1.8, 3.6, 5.5, and 7.2 - 8.0 μm for a growth
198 time of 30, 60, 90, and 120 min, respectively. Consequently, much longer CNFs are possible
199 to be attained once a longer growth time (e.g., > 120 min) is applied or a higher C_2H_2
200 concentration (e.g., > 500 mbar) is used.

201 Prior to employing CNFs/BDD hybrid films as the capacitor electrodes, their wettability
202 was checked. The as-grown CNFs/BDD hybrid films were not water-wettable. This is
203 characteristic of the CNFs. these CNFs was then wet-chemically treated via immersing them
204 in a mixture of H_2SO_4 and HNO_3 (v/v=3:1) for 30 minutes. As a case study, the wettability of
205 CNFs with $t_{\text{Cu,s}}$ of 60 s WOA (**Figure 1b**) was examined. The detected static contact angle of
206 water on the as-grown CNFs is $110.4^\circ \pm 1.0^\circ$ (**Figure S8a**), revealing its hydrophobic nature.
207 Its XPS survey spectrum (**Figure S8c**) exhibits the C 1s (98.1 atom-%) and O 1s (1.9 atom-
208 %) signals at 284.0 and 532.0 eV, respectively. After such a wet-chemical treatment, the
209 contact angle of water on the treated CNFs surface is changed to be $24.0^\circ \pm 0.6^\circ$ (**Figure S8b**).
210 Accordingly, the oxygen content estimated from its XPS survey spectrum rises to 11.6 atom-
211 % (**Figure S8d**). Therefore, the wet-chemical treatment enhances the content of oxygen on
212 the surface of CNFs. The enhanced degree of the hydrophilic terminations then leads to
213 significantly improved wettability of CNFs/BDD hybrid films in aqueous solution. Such a
214 wet-chemical treatment was then always applied for the CNFs used for electrochemical
215 experiments.

216 To optimize the CNFs/BDD hybrid films for the later construction of both EDLCs and
217 PCs, cyclic voltammograms (CVs) of different CNFs/BDD hybrid films were recorded in 1.0
218 M H₂SO₄ at a scan rate of 100 mV s⁻¹. For the growth of these films, $t_{\text{Cu,s}}$ were varied from 15
219 to 120 s. Within investigated CNFs/BDD hybrid films, half of them were grown using
220 annealed copper films (WA) as the catalysts, the rests were grown using those copper films
221 without annealing (WOA) as the catalysts. The growth time for these CNFs was 60 min. For
222 these tests, a three-electrode system was used. **Figure S9a** shows two typical CVs for
223 CNFs/BDD WA and WOA films with $t_{\text{Cu,s}}$ of 60 s. At the same potential, the capacitive
224 current of the CNFs/BDD hybrid film WOA is larger, an indication of a higher capacitance.
225 **Figure S9b** summarizes the calculated capacitances of all CNFs/BDD hybrid films as a
226 function of $t_{\text{Cu,s}}$. These capacitances were estimated from their correspondent CVs. In the case
227 of CNFs/BDD hybrid films WA, almost no variation of capacitances is observed when
228 different $t_{\text{Cu,s}}$ is applied. The nearly unchanged capacitances suggest the constant electrode
229 areas of these CNFs. By using CNFs/BDD hybrid films WOA, the magnitude of the
230 capacitance improves with an increase of $t_{\text{Cu,s}}$ up to 60 s and then remains almost constant
231 until 90 s. On the contrary, a further increase of $t_{\text{Cu,s}}$ longer than 90 s leads to a decrease of the
232 magnitude of the capacitance. Again, the change of the capacitance reflects directly the
233 variation of surface areas of the formed CNFs/BDD hybrid films WOA. For $t_{\text{Cu,s}}$ in the range
234 from 60 to 90 s, the highest capacitance (about 36 mF cm⁻²) is achieved. For further
235 capacitance investigation, CNFs/BDD hybrid films WOA grown with a relatively shorter
236 copper sputter time (e.g., $t_{\text{Cu,s}} = 60$ s) were chosen as EC capacitor electrodes.

237 To reveal the structures of these CNFs, they were further examined with TEM and
238 Raman. **Figure 2a** shows one representative TEM image of a CNF, whose lateral size is about
239 200 nm. The black triangle inside the CNF is a Cu catalyst. Its selected area electron
240 diffraction (SAED) pattern of the [110] zone axis is shown in the inset of **Figure 2a**, proving
241 good crystallinity of a Cu catalyst. **Figure 2b** shows the high magnification of the interface

242 between a Cu catalyst and a CNF, where graphite is formed around the Cu catalyst. Lattice
243 fringes with a distance of about 0.34 nm of the CNF are seen from the high resolution TEM
244 (HRTEM) image of **Figure 2c**, confirming the formation of graphene-like layers around the
245 Cu catalyst.^[10] In the region far away the Cu catalyst the characteristics of amorphous carbon
246 are detected, based on the HRTEM image and the fast Fourier transformation (FFT) image
247 showed in **Figure 2d**. In addition, observation of a large number of the CNFs confirms that
248 graphitization only occurs in the region around the Cu catalyst.



249 **Figure 2.** Characterization: (a) TEM image of a CNF with a Cu catalyst. The inset shows the
250 SAED pattern of the Cu catalyst. (b) TEM image of the interface between a CNF and a Cu
251 catalyst. (c) High-magnification TEM image of image b. The inset reveals the lattice fringes
252 of graphite. (e) HRTEM and FFT (inset) images of the amorphous phase in the CNF.

254

255 A Raman spectrum of the CNFs/BDD hybrid film (**Figure S10**) reveals two major
256 Raman bands: D band at $\sim 1370\text{ cm}^{-1}$ and G band at $\sim 1650\text{ cm}^{-1}$. The D band is attributed to
257 the disordered structure or defects of graphitic sheets. The broad peak observed at around
258 2800 cm^{-1} is probably related to the 2D band of graphite layers. Furthermore, the G band
259 indicates the crystalline graphitic structure.^[11] The ratio of the intensity of the G band (I_G) to
260 that of D band (I_D) is known to be proportional to the graphitization degree of carbon
261 materials. In our case, the value of I_G/I_D , calculated using Gaussian fitting of two peaks, is
262 about 0.42, confirming the large amount of amorphous phases and relatively few graphitic
263 crystallites in the CNFs.^[10]

264 The existence of graphite and Cu inside the CNFs improves the electrical conductivity of
265 the formed material. A more detailed study of the conductivity using scanning tunneling
266 microscope (STM) is still under investigation. Together with its large surface area and a
267 porous structure, CNFs/BDD hybrid films with $t_{\text{Cu,s}}$ of 60 s WOA are expected to facilitate ion
268 transfer in the solution and electron mobility on the interface of a CNFs/BDD electrode.

269

270 **2.2. Performance of CNFs/BDD ECs**

271 *2.2.1. Capacitance*

272 The CNFs/BDD hybrid film with $t_{\text{Cu,s}}$ of 60 s WOA was employed as the capacitor electrode
273 to fabricate ECs. Its capacitances were first studied using a three-electrode system. For the
274 construction of EDLCs, its cyclic voltammograms (CVs) in 1.0 M H_2SO_4 were recorded
275 within the potential range of 0 - 1.0 V at different scan rates (**Figure S11a**). The CVs are
276 nearly rectangular, indicating ideal EDLC behavior. The slight deviation of the CVs from
277 rectangular shape is due to the altered charge transfer resistance (R_{ct}) between CNFs pores and
278 electrolyte interfaces as well as a generated over-potential.^[12] The estimated capacitances are
279 36.4, 48.2, 80.1, and 116.3 mF cm^{-2} at the scan rate of 100, 50, 20, and 10 mV s^{-1} ,
280 respectively. **Figure S11b** presents the galvanostatic charging/discharging (GCD) curves at

281 current densities ranging from 2 to 20 mA cm⁻². At high current densities, the curves are
282 almost symmetrical, demonstrating high reversibility of this EDLC. The IR drop observed at
283 the scan rate of 2 mA cm⁻² is probably due to the internal resistance of CNFs films and R_{ct}
284 caused mainly by diffusion kinetics of the ions. The calculated capacitances are 17.6, 27.7,
285 56.6, and 137.9 mF cm⁻² at the current density of 20, 10, 5, and 2 mA cm⁻², respectively.

286 The CNFs/BDD PCs were then fabricated by introducing redox species (here 0.05 M
287 Fe(CN)₆^{3-/4-}) into 1.0 M Na₂SO₄ aqueous solution. **Figure S11c** shows the CVs recorded in a
288 potential window of -0.2 – 0.8 V at different scan rates. At all scan rates, the CV curves show
289 a pair of redox waves corresponding to the redox reaction of [Fe(CN)₆]³⁻ + e⁻ ↔ [Fe(CN)₆]⁴⁻.
290 The peak potential separation (ΔE_p) is relatively small (e.g., $\Delta E_p = 96$ mV at a scan rate of 10
291 mV s⁻¹). Moreover, the anodic peak currents are identical to the absolute values of the
292 cathodic ones, indicating the excellent reversibility of these PCs. The evaluated capacitances
293 are 35.0, 52.5, 94.8, and 136.8 mF cm⁻² at the scan rate of 100, 50, 20, and 10 mV s⁻¹,
294 respectively. The related GCD curves are shown in **Figure S11d**. All these recorded curves
295 show nonlinear behavior with plateaus, relating to redox reactions of Fe(CN)₆^{3-/4-}. The times
296 for the charging and discharging processes are almost identical at all current densities, again
297 demonstrating perfect reversibility of this PC. The estimated capacitances are 14.5, 34.7, 84.6,
298 and 232.0 mF cm⁻² at the current density of 20, 10, 5, and 2 mA cm⁻², respectively.

299 At high scan rates (e.g., 100 mV s⁻¹) and high current densities (e.g. 20 mA cm⁻²), the
300 capacitances of a PC are slightly smaller than those of an EDLC. Besides two different charge
301 storage mechanisms (namely charge accumulation for EDLCs, charge transfer and
302 accumulation for PCs), there exist additional aspects. First, different supporting electrolytes
303 are employed for these ECs. Namely, the supporting electrolyte used for PCs is Na₂SO₄, while
304 for EDLCs H₂SO₄ is applied as the electrolyte. To clarify the effect of these electrolytes, the
305 CVs of an EDLC in 1.0 M H₂SO₄ and in 1.0 M Na₂SO₄ were recorded at the scan rate of 100
306 mV s⁻¹ (**Figure S12**). The capacitive current obtained in 1.0 M Na₂SO₄ is much smaller,

307 resulting in a low capacitance of 8.3 mF cm^{-2} . The difference can be interpreted as altered
308 conductivity of the electrolytes. For the electrolyte of $1.0 \text{ M H}_2\text{SO}_4$, the conductivity is 1000
309 mS cm^{-1} . For the electrolyte of $1.0 \text{ M Na}_2\text{SO}_4$, it is only 80 mS cm^{-1} .^[13] Moreover, the size of
310 Na^+ ions in hydrated state is larger than that of hydrated protons. The mobility of Na^+ ions in
311 the solution is slower. Their accessibility and accumulation to the pores of the densely packed
312 CNFs are thus hindered. If one compares the capacitance of the EDLC using Na_2SO_4 with that
313 of a PC, the capacitance of a PC is enlarged for more than 4 times even at high scan rates (e.g.,
314 100 mV s^{-1}). Such enhancement of the capacitance is similar or even better than those
315 reported by using other porous carbon materials.^[14] Second, the inferior behavior of the PC at
316 high scan rates or current densities can be attributed to kinetically unfavorable diffusion of
317 ions inside the narrow pores because of slow Na^+ ionic motion and low conductivity of the
318 electrolyte, leading to loss of the full contribution of active surface area of a CNF film.

319 To figure out clearly the contribution of CNFs into the construction of these ECs, the
320 capacitance of the fabricated EDLC is compared with that of reported EDLCs constructed
321 using diamond nanostructures or hydride films of BDD with carbon materials (**Figure S13**).
322 Clearly, BDD nanostructures (e.g., honeycomb diamond,^[15] porous diamond,^[16] and diamond
323 networks,^[17] etc.) own enhanced surface areas and thus exhibit significantly improved
324 capacitances in comparison to flat BDD films. The hybrid films of BDD with other carbon
325 materials (e.g., carbon nanotube,^[18] carbon fiber,^[19] etc.) also deliver larger capacitances than
326 BDD EDLCs. This is attributed partially to further increased surface areas, partially to the
327 addition of the capacitances from other carbon materials. Compared with these values, the
328 capacitance of CNFs/BDD EDLC in this study is the highest. Moreover, the comparison of
329 the capacitances of different diamond PCs is shown in **Figure S13**. The capacitance of the
330 CNFs/BDD PC reaches the highest value of 232.0 mF cm^{-2} . It is much larger than that of
331 metal oxide (e.g. Ni(OH)_2 ^[20]), conducting polymer (e.g. PEDOT^[21]), and diamond nanowires
332 based PCs. It is also higher than that when a diamond network was utilized as the capacitor

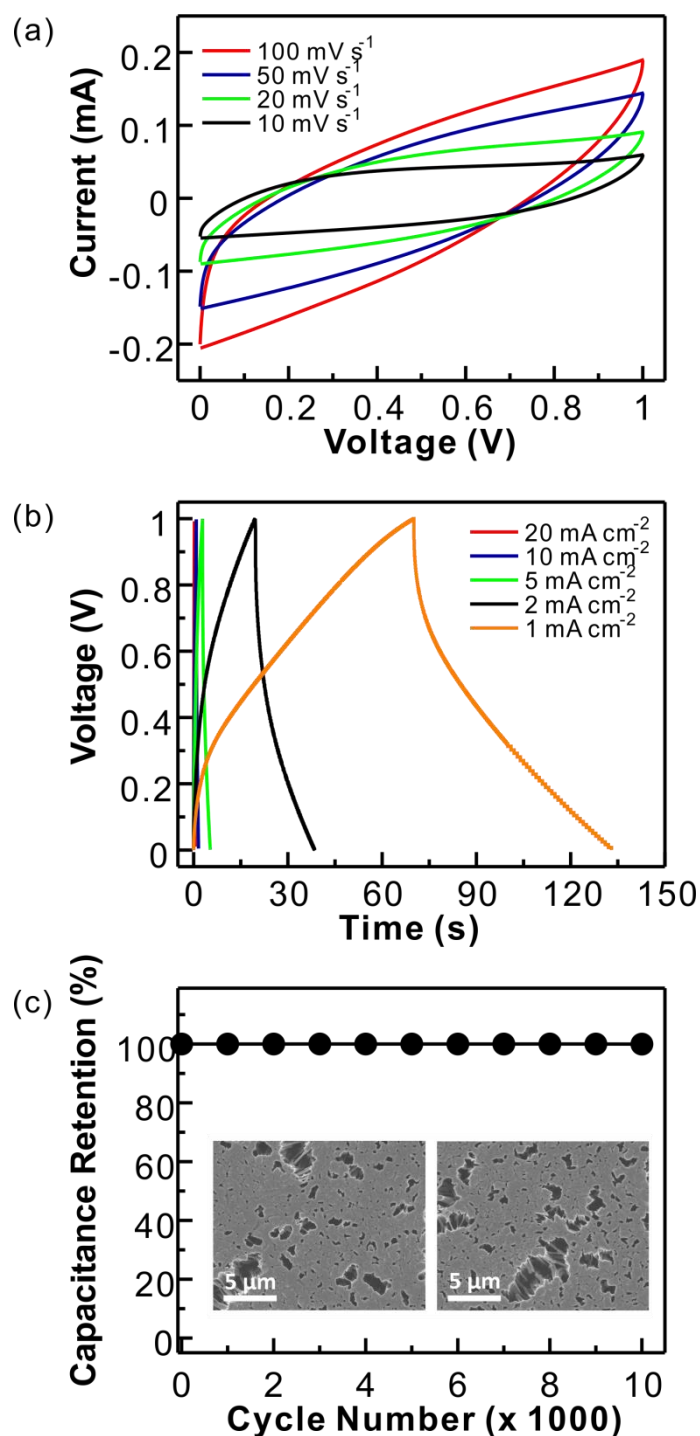
333 electrode and the redox solution was the electrolyte.^[17a] In summary, the large surface area,
334 the improved electrical conductivity, and the unique porous structure of these vertically
335 aligned CNFs on BDD lead to the high-performance of these EDLCs and PCs.

336 The effect of the growth time of CNFs on the capacitances of CNFs/BDD hybrid films
337 were also examined in 1.0 M H₂SO₄ using a three-electrode system. The CVs of CNFs with a
338 growth time of 30, 90, and 120 min were recorded at a scan rate of 100 mV s⁻¹ (**Figure S14a**).
339 The capacitances calculated from the related CVs are listed in **Figure S14b**. The magnitude of
340 the capacitance improves almost linearly with an increase of growth time of CNFs. This is
341 because the lengths of CNFs, namely the surface area of a CNF film, are enhanced nearly
342 linear of as a function of the growth time. In other words, the capacitance of these CNFs/BDD
343 ECs is possible to be further improved as required only through applying longer TCVD
344 growth times.

345 For practical applications of these ECs, a two-electrode symmetrical supercapacitor
346 device was assembled. Two CNFs/BDD hybrid films were used as the capacitor electrodes.
347 These films were grown with $t_{\text{Cu,s}}$ of 60 s WOA. The performance of as-fabricated ECs was
348 first investigated in 1.0 M H₂SO₄ aqueous solution. **Figure 3a** shows the CV curves recorded
349 at the scan rates of 100, 50, 20, and 10 mV s⁻¹ and with a cell voltage of 1.0 V. Similar as the
350 results obtained by a three-electrode system, CVs show nearly rectangular shape at low scan
351 rates, revealing good double layer capacitive behavior. The calculated capacitances are 7.7,
352 11.7, 21.6, and 30.4 mF cm⁻² at the scan rate of 100, 50, 20, and 10 mV s⁻¹, respectively.

353 The related GCD curves of the EDLC device recorded at the current densities from 1 to
354 20 mA cm⁻² are presented in **Figure 3b**. The curves are almost symmetric at high current
355 densities, demonstrating the high reversibility of the EC. When lower current densities (here
356 smaller than 2 mA cm⁻²) are applied, asymmetrical curves are acquired, due to the charge
357 transfer resistance at the electrode and electrolyte interfaces. The times required for charging
358 and discharging processes are almost equivalent, indicating a high columbic efficiency of the

359 EDLC. The calculated capacitances are 2.1, 4.0, 6.8, 19.6, and 34.0 mF cm⁻² at the current
 360 density of 20, 10, 5, 2, and 1 mA cm⁻², respectively.



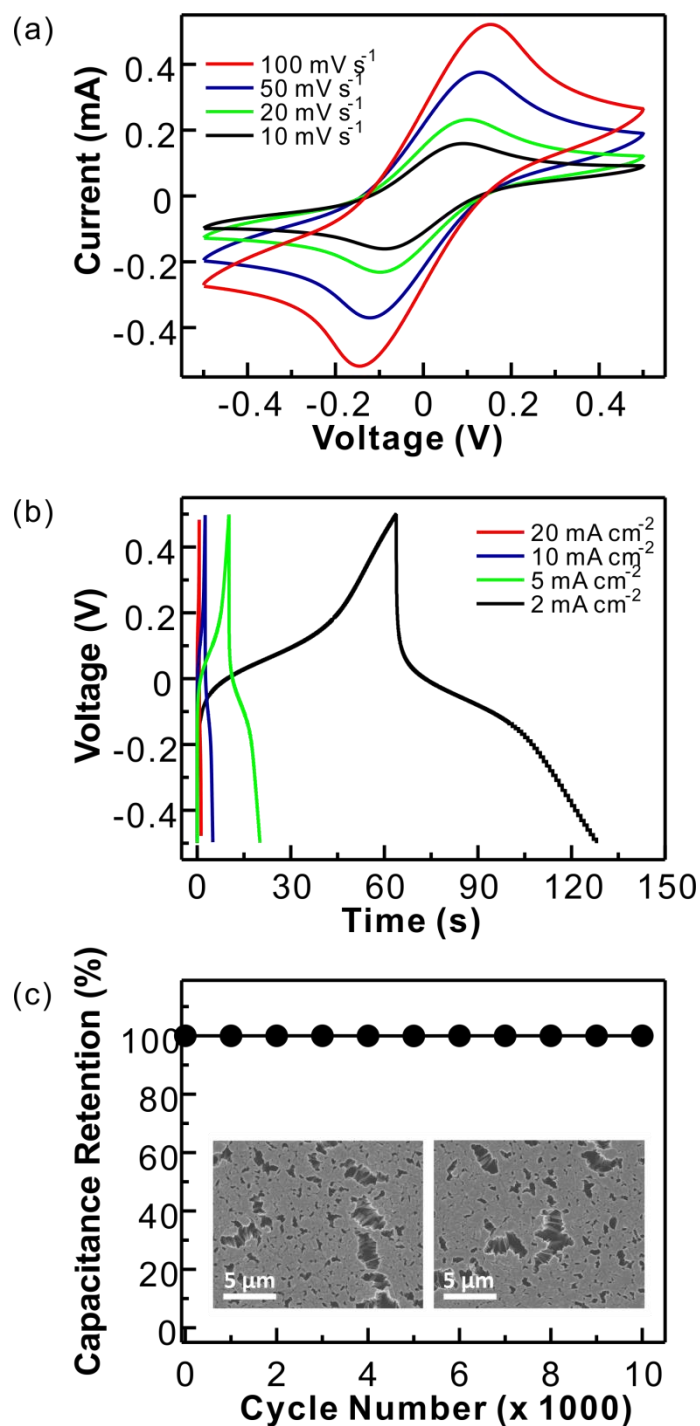
361
 362
 363 **Figure 3.** Performance of a CNFs/BDD symmetric EDLC device in 1.0 M H₂SO₄: (a) CVs
 364 recorded at the scan rates of 100, 50, 20, and 10 mV s⁻¹; (b) Charging/discharging curves at
 365 the current densities of 1, 2, 5, 10, and 20 mA cm⁻²; (c) Capacitance retention at the
 366 charging/discharging current density of 5 mA cm⁻². The inset SEM images show the

367 morphologies of two used CNFs/BDD hybrid films after 10 000 charging/discharging cycles.

368 Considering that fast charging/discharging processes are required for ECs, CV
369 measurements at high scan rates (e.g., up to 3 V s^{-1}) were carried out. The related CVs are
370 displayed in **Figure S15a**. Deformation of the CV curves is noticed at these high scan rates.
371 This is quite normal due to insufficient time for ion adsorption/desorption and diffusion into
372 the inner pores. In this context, the capacitance decreases with an increase of the scan rate, as
373 shown in **Figure S15b**. Consequently, these CNFs/BDD EDLCs are possible to be applied for
374 fast charging/discharging processes.

375 On the other hand, the capacitance of a PC device was then evaluated in a cell voltage of
376 $-0.5 - 0.5 \text{ V}$ in $1.0 \text{ M Na}_2\text{SO}_4$ solution containing $0.05 \text{ M Fe(CN)}_6^{3-/4-}$. At all scan rates, the
377 CV curves (**Figure 4a**) show a pair of well-defined peaks, relating to the redox reaction of
378 $\text{Fe(CN)}_6^{3-/4-}$. In addition, the integrated charges from the anodic and cathodic cycles evidence
379 that the charges stored on the electrodes during a charging process are nearly identical to
380 those removed during a discharging process. The calculated capacitance are 15.7, 23.3, 36.1,
381 and 48.1 mF cm^{-2} at the scan rate of 100, 50, 20, and 10 mV s^{-1} , respectively.

382 **Figure 4b** presents the GCD curves of this PC device at different charging/discharging
383 current densities. The plateaus in the curves are relative to the redox reactions of $\text{Fe(CN)}_6^{3-/4-}$.
384 Almost same times are required for charging and discharging processes even at a low current
385 density of 2 mA cm^{-2} . The estimated columbic efficiency is about 100%, confirming the
386 excellent reversibility of such a PC device. The calculated capacitances are 6.4, 12.8, 25.6,
387 and 65.4 mF cm^{-2} at the current density of 20, 10, 5, and 2 mA cm^{-2} , respectively.



388
 389
 390 **Figure 4.** Performance of a CNFs/BDD symmetric PC device in 0.05 M Fe(CN)₆^{3-/4-} + 1.0 M
 391 Na₂SO₄: (a) CVs at the scan rates of 100, 50, 20, and 10 mV s⁻¹; (b) Charging/discharging
 392 curves at the current densities of 2, 5, 10, and 20 mA cm⁻²; (c) Capacitance retention at the
 393 charging/discharging current density of 10 mA cm⁻². The inset SEM images show the surface
 394 characteristics of two used CNFs/BDD hybrid films after 10 000 charging/discharging cycles.

395 Interestingly, the capacitance of a PC device is several times larger in comparison to that of an
396 EDLC device. Such an enlarged capacitance is sum of both electrical double layer capacitance
397 and pseudocapacitance. The former results from the charge/ion accumulation on the surface of
398 CNFs/BDD films. The latter originates from the rapid occurrence of faradaic reaction of
399 $[\text{Fe}(\text{CN})_6]^{3-} + e^- \leftrightarrow [\text{Fe}(\text{CN})_6]^{4-}$ on the CNFs/BDD interfaces. Moreover, when soluble redox
400 species of $\text{Fe}(\text{CN})_6^{3-/4-}$ are added in the electrolyte, the charge-transfer resistance at the
401 CNFs/BDD interfaces is expected to be reduced, but the ionic conductivity of the solution is
402 expected to be enhanced. Those results are similar with those obtained on diamond
403 networks.^[17a] This pseudocapacitance is thus much higher than that of the electrical double
404 layer capacitance. In short, both fabricated CNFs/BDD EDLC and PC devices feature the
405 characteristics of battery-like supercapacitors, in this case a large capacitance.

406

407 2.2.2. Capacitance retention

408 The cycling stability of a CNFs/BDD EDLC device was further examined using GCD
409 technique at the current density of 5 mA cm^{-2} . After 10 000 cycles, the capacitance remains
410 unchanged (**Figure 3c**). The morphologies of both capacitor electrodes were then checked
411 after the lifetime test. Their SEM images are shown in the insets of **Figure 3c**. In comparison
412 to that of as grown CNFs films shown in **Figure 1b**, neither obvious surface damages nor
413 differences regarding surface morphology or porosity are observed, demonstrating the
414 excellent stability of the CNFs/BDD capacitor electrode.

415 For the cycling stability test of a CNFs/BDD PC device, a long time
416 charging/discharging process (e.g., for 10 000 cycles) was carried out using GCD technique at
417 the current density of 10 mA cm^{-2} . The capacitance retention as a function of the cycle
418 number is shown in **Figure 4c**, illustrating that the initial capacitance maintains unchanged
419 after the lifetime test. The surface morphologies of two electrodes (the inset of **Figure 4c**)
420 show almost no change, compared to the as grown CNFs films (**Figure 1b**), again

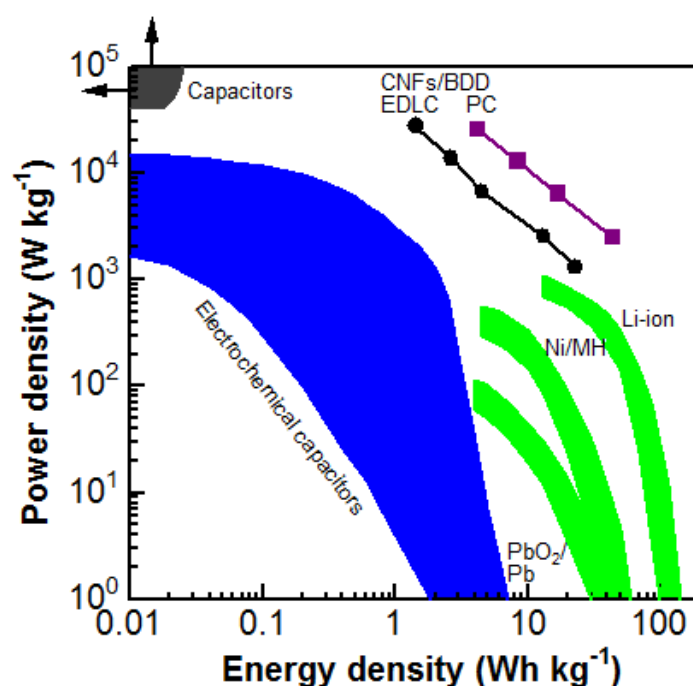
421 demonstrating the perfect stability of the electrodes and also a high degree of the reversibility
 422 in the electrolyte.

423 Therefore, the CNFs/BDD based EDLC and PC devices have long-term cycle ability,
 424 one of the important advantages of battery-like supercapacitors.

425

426 2.2.3. Energy and Power Densities

427 To clarify the overall performance of the CNFs/BDD EC devices, their energy and power
 428 densities were further calculated. The related Ragone plots are displayed in **Figure 5**. The
 429 estimated maximal E and P reach the values of 22.9 W h kg^{-1} and 27.3 kW kg^{-1} for an EDLC
 430 device, respectively. While for a PC device, they are 44.1 W h kg^{-1} and 25.3 kW kg^{-1} ,
 431 respectively. Compared to other energy devices (e.g., ECs, batteries, etc.^[22]) shown in **Figure**
 432 **5**, the proposed CNFs/BDD EC devices exhibit not only much higher P , but also higher E
 433 than those of some reported supercapacitors. The value of E is similar to that of batteries. The
 434 reason is ascribed to the structure of the electrodes and also the “battery-like” behavior of the
 435 $\text{Fe}(\text{CN})_6^{3-/4-}$ redox electrolyte.^[17a]



436
 437

Figure 5. Performance of a CNFs/BDD EC device in both inert solution and redox electrolyte:

438 Ragone plots of CNFs/BDD EDLCs (closed dots) and PCs (closed squares) in comparison
439 with those^[22] of traditional capacitors, ECs and batteries. Reproduced with permission.^[22]
440 Copyright 2008, Macmillan Publishers Limited.

441
442 **Table S1** further compares the performance (e.g., E and P) of our CNFs/BDD EC
443 devices with that of other CNFs based EC devices reported in the literature. The E and P
444 values of our CNFs/BDD EC devices are higher than those of many reported CNFs based EC
445 devices.^[23] For instance, porous CNFs based EDLC devices only show an E of 17 W h kg^{-1}
446 and a P of 20 kW kg^{-1} .^[24] The E and P of EDLC devices fabricated by N,P – co-doped CNFs
447 networks reach the values of 7.8 W h kg^{-1} and 26.6 kW kg^{-1} , respectively.^[25] By applying
448 $\text{V}_2\text{O}_5/\text{CNFs}$ composites as electrode material, the PC devices exhibit an E of 18.8 W h kg^{-1} , as
449 well as a P of 20.0 kW kg^{-1} .^[26]

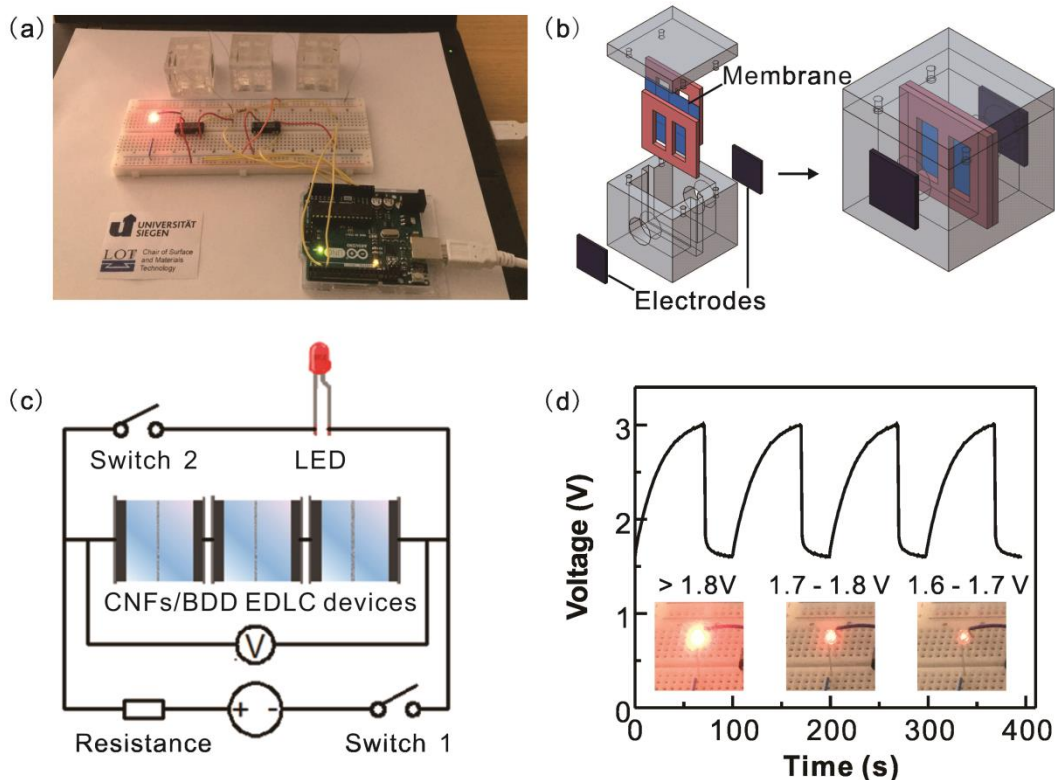
450 In conclusion, both EDLC and PC devices fabricated from the CNFs/BDD capacitor
451 electrodes exhibit high power densities and high energy densities. They are characteristic for
452 battery-like supercapacitors. Together with obtained large capacitances, long-term
453 capacitance retention, battery-like EDLCs and PCs are successfully formed using vertically
454 aligned carbon nanofibers grown on BDD as the capacitor electrodes.

455 456 2.2.4. Battery-like Supercapacitor Demonstrator

457 A stand-alone and portable system was designed to demonstrate the proposed CNFs/BDD
458 ECs for practical applications. The built demonstrator (**Figure 6a**) consists of three EDLC
459 devices assembled in series, a single-board microcontroller to control the
460 charging/discharging processes, a red LED (working voltage: 1.8 V), and a USB cable to
461 charge this device. The designed prototype of a CNFs/BDD EC device is schematically
462 illustrated in **Figure 6b**. Two CNFs/BDD capacitor electrodes are attached tightly to both
463 sides of the cell, made from transparent acrylic glass. The efficient area of each electrode

464 exposed to the electrolyte is about 0.785 cm^2 . A $50 \text{ }\mu\text{m}$ Nafion membrane is fixed with two
465 sheets in the middle of the cell. As a case study, the electrolyte ($1.0 \text{ M H}_2\text{SO}_4$) was filled in
466 the cell from the top.

467 **Figure 6c** shows the electrical circuit diagram of such a demonstrator. In the first step,
468 the switch '1' is closed, the devices are charged by an external power supplier with the USB
469 connector. The resistance in the circuit is used to adjust the charging current, or charging
470 duration. When the measured voltage of the EC devices is up to 3 V , the switch '1' opens and
471 then the switch '2' is closed, leading to powering and illuminating a commercial red LED.
472 Moreover, the discharge process of the EC devices is possible to be tested. When the voltage
473 is lower than 1.6 V , the switch '2' opens and the switch '1' is closed, and the EC devices are
474 charged again. Such a process is automatically controlled by a single-board microcontroller.
475 In other words, such ECs are also possible to be charged by connecting to a computer or a
476 power supplier with the USB connector (**Figure 6a**). **Figure 6d** shows the variation of
477 voltages in the recorded curves during the charging/discharging processes as a function of
478 time. The good repeatability of the curves reveals the excellent reversibility and stability of
479 the device. With a charge time of about 70 s , the red LED lights up (**Figure 6d**). The light
480 intensity is varied as a function of the applied voltages (the insets in **Figure 6d**). With a high
481 voltage at an initial stage, the LED is very bright, indicating the capacitor features of ECs.
482 The light lasts for few seconds and becomes weaker till it ceases. Therefore, the fabricated
483 battery-like supercapacitors made from CNFs/BDD hybrid films are promising for the
484 employment of practical energy storage applications.



485
 486 **Figure 6.** A stand-alone CNFs/BDD EC demonstrator: (a) a photograph of the demonstrator
 487 consisting of three CNFs/BDD EDLC devices in series, a single-board microcontroller
 488 connected to the computer with a USB cable, and a red LED; (b) the design of a CNFs/BDD
 489 EC prototype used in the system; (c) the schematic electrical circuit diagram related to (a); (d)
 490 typical curves of the voltage as a function of time during the charging/discharging processes.
 491 The insets show the variation of light intensity of the red LED in relation to the cell voltage.

492

493 3. Conclusion

494 Vertically aligned carbon nanofibers directly grown on BDD, novel hybrid carbon materials,
 495 have been utilized as the capacitor electrodes to develop supercapacitors. Both electrical
 496 double layer capacitors using inert solutions and pseudocapacitors using redox electrolytes
 497 have been fabricated. These ECs feature large capacitance (in the range of mF cm^{-2}), long-
 498 term capacitance retention, high power densities, and high energy densities. Such high energy
 499 and power densities achieved from the CNFs/BDD EC devices are superior to those of
 500 reported batteries and supercapacitors. The high performance of these battery-like ECs is

501 attributed to the large surface areas, improved electrical conductivity, and porous structures of
502 these binder-free CNFs/BDD hybrid films. Their performance is possible to be further
503 enhanced only with longer CNFs (e.g., simply by applying a longer growth time). Future
504 research activities can be focused on the employment of water-soluble but multi-electrons
505 transferred redox electrolyte (e.g., heteropolyacids) as well as ionic redox electrolytes for the
506 construction of battery-like supercapacitors. By use of these redox electrolytes, the improved
507 performance of battery-like capacitors is expected, including their capacitances, capacitance
508 retention, as well as power and energy densities. Moreover, these battery-like supercapacitors
509 should be constructed at the large scales on the flexible substrates (e.g., carbon clothes).
510 Together with the stand-alone demonstrator, the battery-like supercapacitors will be
511 promising and possible for powering future multifunctional electronics, hybrid electric
512 vehicles, and industrial equipments in near future.

513

514 **4. Experimental Section**

515 *Electrode materials:* **Figure S1** illustrates schematically the steps for the growth of
516 CNFs/BDD hybrid films using a TCVD technique. First, BDD films were grown on silicon
517 wafers using microwave plasma assisted chemical vapor deposition (MWCVD) technique.^[27]
518 Then, the coating of BDD with copper films was carried out on a PVD device. A high purity
519 (99.999%) copper disk (4 inch in diameter) was used as the source material. The RF
520 magnetron sputtering tool was equipped with a turbo molecular pump and its base pressure
521 was lower than 5×10^{-6} mbar. Prior to coating, a pre-sputtering of the target for 10 min with a
522 closed shutter was applied to clean the target. Applied coating conditions were: the substrate
523 at room temperature, argon atmosphere, an argon gas flow of 50 sccm, a pressure of $3.5 -$
524 4.5×10^{-3} mbar. The thickness of copper films on BDD was varied through altering $t_{\text{Cu,s}}$. In this
525 study, $t_{\text{Cu,s}}$ was varied from 15, 30, 60, 90, to 120 s. After that, copper coated BDD films were
526 introduced in the center of a quartz tube in a TCVD device. To grow CNFs, these sputtered

527 copper films were utilized as the catalysts. At a pressure of about 5×10^{-2} mbar, the tube was
528 heated to 250 °C with a heating rate of 5 °C min⁻¹. Subsequently, the reaction gas of C₂H₂ was
529 filled into the tube till a pressure of 500 mbar was reached. The growth times were varied
530 from few minutes to few hours. After the growth, the reactor was rapidly evacuated. Once the
531 pressure in the tube was lower than 5×10^{-2} mbar, the carbonization of CNFs was carried out.
532 The carbonization temperature was 800 °C and the time applied was 60 min. As control
533 experiments, copper films were annealed before the growth of CNFs in the TCVD device
534 under the conditions of an annealing temperature of 500 °C, a pressure of about 5×10^{-2} mbar,
535 and an annealing time for 60 min. To change the wettability of CNFs/BDD hybrid films, they
536 were immersed in a mixture of H₂SO₄ and HNO₃ (v/v = 3:1) for 30 min, then cleaned with
537 deionized water, and finally dried in a N₂ atmosphere before the electrochemical experiments.

538 *Characterization:* The surface and cross section morphologies of CNFs/BDD hybrid
539 films were investigated with field emission scanning electron microscopy (FESEM, Zeiss
540 Ultra55, Germany). The Raman spectra of these films were recorded on a homemade micro
541 Raman configuration with a 532 nm laser. An X-ray photoelectron spectroscopy (XPS,
542 Surface Science Instruments, SSX-100 S-probe photoelectron spectrometer, USA) with an Al
543 K α radiation of 200 W was used to characterize the elemental composition of these films.
544 Static contact angle measurements were carried out on an OCA 15plus instrument (Data
545 Physics Instruments GmbH, Filderstadt, Germany) with Milli-Q water drawn from a Millipore
546 Direct Q8 system (Millipore, Schwalbach, with Millimark Express 40 filter, Merck, Germany)
547 with a resistivity of 18.0 M Ω cm. The nanostructure of CNFs was further examined with
548 transmission electron microscopy (TEM, FEI Tecnai G2 F30, USA). CNFs were collected via
549 mechanical scratching from the BDD and then dispersed in ethanol. Subsequently, the ethanol
550 containing nanostructures were dropped on a thin carbon film covered copper grid using a
551 drip pipe. After drying, the copper grid was examined under TEM.

552 *Electrochemical measurements:* Electrochemical measurements were conducted on a
553 CHI660E Potentiostat / Galvanostat (Shanghai Chenhua Inc., China). A standard three-
554 electrode cell was utilized where a CNFs/BDD hybrid film acted as the working electrode, an
555 Ag/AgCl (3 M KCl) electrode as the reference electrode, and a coiled Pt wire as the counter
556 electrode. In a two-electrode symmetrical supercapacitor device, two CNFs/BDD hybrid films
557 were served as the capacitor electrodes and a 50 μm thick Nafion[®] film (Alfa Aesar) as the
558 separator. The geometric area of a CNFs/BDD hybrid capacitor electrode was 0.05 cm^2 . For
559 EDLCs, the electrolyte was 1.0 M H_2SO_4 . For PCs, the electrolyte was 1.0 M Na_2SO_4
560 containing 0.05 M $\text{K}_3\text{Fe}(\text{CN})_6/\text{K}_4\text{Fe}(\text{CN})_6$. The cyclic voltammograms (CVs) were recorded
561 at the scan rates ranging from 10 to 100 mV s^{-1} . The galvanostatic charging/discharging
562 (GCD) curves for EDLCs and PCs were obtained at different current densities. The specific
563 capacitances (C , F cm^{-2}), energy density (E , Wh kg^{-1}), and power density (P , W kg^{-1}) of ECs
564 were calculated according to the reported methods.^[17a, 28]

565

566

567 **Supporting Information**

568 Supporting Information is available from the Wiley Online Library or from the author.

569

570 **Acknowledgements**

571 S.Y. gratefully acknowledges the financial support from China Scholarship Council (Chinese
572 Government Scholarship, Award no. 201408080015). N.Y. acknowledges the financial
573 support from the German Research Foundation (DFG) under project YA344/1-1. H.S.
574 acknowledges financial support from the European Research Council (ERC project
575 ASMIDIAS, Grant no. 279202) and the University of Siegen.

576

577

Received: ((will be filled in by the editorial staff))

578

Revised: ((will be filled in by the editorial staff))

579

Published online: ((will be filled in by the editorial staff))

580 References

- 581 [1] a) W. Zuo, R. Li, C. Zhou, Y. Li, J. Xia, J. Liu, *Adv. Sci.* **2017**, *4*, 1600539; b) T.
582 Brousse, D. Bélanger, J. W. Long, *J. Electrochem. Soc.* **2015**, *162*, A5185; c) C.
583 Costentin, T. R. Porter, J.-M. Savéant, *ACS Appl. Mater. Interfaces* **2017**, *9*, 8649.
- 584 [2] a) P. F. Smith, K. J. Takeuchi, A. C. Marschilok, E. S. Takeuchi, *Acc. Chem. Res.*
585 **2017**, *50*, 544; b) L.-F. Chen, Y. Lu, L. Yu, X. W. Lou, *Energy Environ. Sci.* **2017**, *10*,
586 1777; c) C. Zhu, T. Liu, F. Qian, T. Y.-J. Han, E. B. Duoss, J. D. Kuntz, C. M.
587 Spadaccini, M. A. Worsley, Y. Li, *Nano Lett.* **2016**, *16*, 3448; d) L. Mai, H. Li, Y.
588 Zhao, L. Xu, X. Xu, Y. Luo, Z. Zhang, W. Ke, C. Niu, Q. Zhang, *Sci. Rep.* **2013**, *3*,
589 1718.
- 590 [3] a) J. Liu, L. Zhang, H. B. Wu, J. Lin, Z. Shen, X. W. Lou, *Energy Environ. Sci.* **2014**,
591 *7*, 3709; b) E. Frackowiak, F. Béguin, *Carbon* **2001**, *39*, 937.
- 592 [4] W. Wu, L. Yang, S. Chen, Y. Shao, L. Jing, G. Zhao, H. Wei, *RSC Adv.* **2015**, *5*,
593 91645.
- 594 [5] Y. Wang, Y. Xia, *Adv. Mater.* **2013**, *25*, 5336.
- 595 [6] C. Zhong, Y. Deng, W. Hu, J. Qiao, L. Zhang, J. Zhang, *Chem. Soc. Rev.* **2015**, *44*,
596 7484.
- 597 [7] a) V. Augustyn, P. Simon, B. Dunn, *Energy Environ. Sci.* **2014**, *7*, 1597; b) P. Simon,
598 Y. Gogotsi, B. Dunn, *Science* **2014**, *343*, 1210; c) A. C. Forse, J. M. Griffin, C. Merlet,
599 J. Carretero-Gonzalez, A.-R. O. Raji, N. M. Trease, C. P. Grey, *Nat. Energy* **2017**, *2*,
600 16216; d) C. Prehal, C. Koczwara, N. Jäckel, A. Schreiber, M. Burian, H. Amenitsch,
601 M. A. Hartmann, V. Presser, O. Paris, *Nat. Energy* **2017**, *2*, 16215.
- 602 [8] a) Y. Ma, N. Yang, X. Jiang, in *Carbon Nanoparticles and Nanostructures* (Eds: N.
603 Yang, X. Jiang, D.-W. Pang), Springer International Publishing, Switzerland **2016**, p.
604 47; b) Y. Gao, G. P. Pandey, J. Turner, C. R. Westgate, B. Sammakia, *Nanoscale Res.*
605 *Lett.* **2012**, *7*, 651.

- 606 [9] a) X. Jiang, *Phys. Status Solidi A* **2014**, *211*, 2679; b) J. H. Xia, X. Jiang, C. L. Jia,
607 *Appl. Phys. Lett.* **2009**, *95*, 223110.
- 608 [10] Y. Ma, X. Sun, N. Yang, J. Xia, L. Zhang, X. Jiang, *Chem. -Eur. J.* **2015**, *21*, 12370.
- 609 [11] a) Q. Yong, E. Maik, S. Thorsten, J. Xin, *Nanotechnology* **2007**, *18*, 345607; b) Y. Liu,
610 J. Zhou, L. Chen, P. Zhang, W. Fu, H. Zhao, Y. Ma, X. Pan, Z. Zhang, W. Han, E. Xie,
611 *ACS Appl. Mater. Interfaces* **2015**, *7*, 23515.
- 612 [12] L. Hu, W. Chen, X. Xie, N. Liu, Y. Yang, H. Wu, Y. Yao, M. Pasta, H. N. Alshareef,
613 Y. Cui, *ACS Nano* **2011**, *5*, 8904.
- 614 [13] a) D. Jiménez-Cordero, F. Heras, M. A. Gilarranz, E. Raymundo-Piñero, *Carbon* **2014**,
615 *71*, 127; b) K. Torchała, K. Kierzek, J. Machnikowski, *Electrochim. Acta* **2012**, *86*,
616 260; c) X. Zhang, X. Wang, L. Jiang, H. Wu, C. Wu, J. Su, *J. Power Sources* **2012**,
617 *216*, 290.
- 618 [14] a) S. Roldán, C. Blanco, M. Granda, R. Menéndez, R. Santamaría, *Angew. Chem., Int.*
619 *Ed.* **2011**, *50*, 1699; b) S. Roldán, Z. González, C. Blanco, M. Granda, R. Menéndez,
620 R. Santamaría, *Electrochim. Acta* **2011**, *56*, 3401.
- 621 [15] K. Honda, T. N. Rao, D. A. Tryk, A. Fujishima, M. Watanabe, K. Yasui, H. Masuda, *J.*
622 *Electrochem. Soc.* **2001**, *148*, A668.
- 623 [16] V. Petrák, Z. Vlčková Živcová, H. Krýsová, O. Frank, A. Zukal, L. Klimša, J.
624 Kopeček, A. Taylor, L. Kavan, V. Mortet, *Carbon* **2017**, *114*, 457.
- 625 [17] a) S. Yu, N. Yang, H. Zhuang, S. Mandal, O. A. Williams, B. Yang, N. Huang, X.
626 Jiang, *J. Mater. Chem. A* **2017**, *5*, 1778; b) H. Zhuang, N. Yang, H. Fu, L. Zhang, C.
627 Wang, N. Huang, X. Jiang, *ACS Appl. Mater. Interfaces* **2015**, *7*, 5384.
- 628 [18] C. Hébert, J. P. Mazellier, E. Scorsone, M. Mermoux, P. Bergonzo, *Carbon* **2014**, *71*,
629 27.
- 630 [19] a) E. C. Almeida, A. F. Azevedo, M. R. Baldan, N. A. Braga, J. M. Rosolen, N. G.
631 Ferreira, *Chem. Phys. Lett.* **2007**, *438*, 47; b) E. C. Almeida, M. R. Baldan, J. M.

- 632 Rosolen, N. G. Ferreira, *Diamond Relat. Mater.* **2008**, *17*, 1529.
- 633 [20] F. Gao, C. E. Nebel, *Phys. Status Solidi A* **2015**, *212*, 2533.
- 634 [21] D. Aradilla, F. Gao, G. L. Malandrakis, W. Müller-Sebert, P. Gentile, M. Boniface, D.
635 Aldakov, B. Iliev, T. J. S. Schubert, C. E. Nebel, G. M. Bidan, *ACS Appl. Mater.*
636 *Interfaces* **2016**, *8*, 18069.
- 637 [22] P. Simon, Y. Gogotsi, *Nat. Mater.* **2008**, *7*, 845.
- 638 [23] a) Z. Liu, D. Fu, F. Liu, G. Han, C. Liu, Y. Chang, Y. Xiao, M. Li, S. Li, *Carbon* **2014**,
639 *70*, 295; b) C. H. Kim, B.-H. Kim, *J. Power Sources* **2015**, *274*, 512; c) C. Tran, V.
640 Kalra, *J. Power Sources* **2013**, *235*, 289.
- 641 [24] B.-H. Kim, K. S. Yang, H.-G. Woo, K. Oshida, *Synth. Met.* **2011**, *161*, 1211.
- 642 [25] L.-F. Chen, Z.-H. Huang, H.-W. Liang, H.-L. Gao, S.-H. Yu, *Adv. Funct. Mater.* **2014**,
643 *24*, 5104.
- 644 [26] B.-H. Kim, C. H. Kim, K. S. Yang, A. Rahy, D. J. Yang, *Electrochim. Acta* **2012**, *83*,
645 335.
- 646 [27] a) O. A. Williams, *Diamond Relat. Mater.* **2011**, *20*, 621; b) J. Hees, A. Kriele, O. A.
647 Williams, *Chem. Phys. Lett.* **2011**, *509*, 12; c) O. A. Williams, O. Douhéret, M.
648 Daenen, K. Haenen, E. Ōsawa, M. Takahashi, *Chem. Phys. Lett.* **2007**, *445*, 255; d) W.
649 Gajewski, P. Achatz, O. A. Williams, K. Haenen, E. Bustarret, M. Stutzmann, J. A.
650 Garrido, *Phys. Rev. B* **2009**, *79*, 045206.
- 651 [28] F. Béguin, V. Presser, A. Balducci, E. Frackowiak, *Adv. Mater.* **2014**, *26*, 2219.
- 652